

Structural and Spectroscopic Properties of Pure and Doped $\text{Ba}_6\text{Ti}_2\text{Nb}_8\text{O}_{30}$ Tungsten BronzeV. Massarotti,^{*,†} D. Capsoni,[†] M. Bini,[†] C. B. Azzoni,[‡] M. C. Mozzati,[‡] P. Galinetto,[‡] and G. Chiodelli[§]*Dipartimento di Chimica Fisica, "M. Rolla" dell'Università, viale Taramelli 16, 27100 Pavia, Italy, CNISM - Dipartimento di Fisica, "A. Volta" dell'Università, via Bassi 6, 27100 Pavia, Italy, and CNR - IENI, Sezione di Pavia, viale Taramelli 16, 27100 Pavia, Italy**Received: June 1, 2006; In Final Form: July 13, 2006*

Pure and doped $\text{Ba}_6\text{Ti}_2\text{Nb}_8\text{O}_{30}$ (BTN), obtained by substituting $M = \text{Cr}$, Mn , or Fe on the Ti site ($\text{Ba}_6\text{Ti}_{2-x}\text{M}_x\text{Nb}_8\text{O}_{30}$, $x = 0.06$ and 0.18) and Y and Fe on the Ba and Ti sites, respectively ($\text{Ba}_{6-x}\text{Y}_x\text{Ti}_{2-x}\text{Fe}_x\text{Nb}_8\text{O}_{30}$, $x = 0.18$), are synthesized. The influence of cation doping on the local structure, the cation oxidation state, and the possible defect formation able to maintain the charge neutrality are investigated by spectroscopic (electron paramagnetic resonance (EPR) and micro-Raman), structural (X-ray powder diffraction) and transport (impedance spectroscopy, thermoelectric power) measurements, in the temperature range of 300–1200 K in air and N_2 flow. Starting from the valence state of the doping ions (Fe^{3+} , Cr^{3+} , and Mn^{2+}), determined by EPR, and from thermoelectric power measurements, evidencing a negative charge transport, different charge-compensating defect equilibria, based on the creation of positive electron holes or oxygen vacancies and electrons, are discussed to interpret the conductivity results.

Introduction

Materials with the general formula $\text{A}_6\text{B}_1\text{B}_2\text{O}_{30}$ ($A = \text{Ba}$, $B_1 = \text{Ti}$, $B_2 = \text{Nb}$) can be considered members of the tetragonal space group (SG) $P4bm$ tungsten bronze-type family. These compounds display peculiar ferroelectric, electrooptical, and nonlinear optical properties both in polycrystalline¹ and single crystal² forms. Moreover, their dielectric constant^{2,3} and resistivity⁴ show a non-monotonic trend with temperature, indicating paraelectric–ferroelectric or ferroelectric–ferroelastic transitions. Many papers are also reported in the literature concerning the substitution on the A site of different rare earth materials^{5–9} and Na or $\text{K}^{10–13}$ ions; the charge neutrality is maintained by a suitable change of Ti^{4+} and Nb^{5+} cation stoichiometry. Other substitutions with isovalent ions of Ti and Nb (e.g., Hf or Zr and Ta, respectively) were also recently investigated.¹⁴ In some cases, a wide stability range interval of the formed solid solutions is possible; in other components of the family, the tetragonal structure becomes unstable and a lower orthorhombic symmetry is preferred, as is the case for Ba substitution with Ca, Sr, or Pb ions.^{4,14}

The crystal structure of $\text{Ba}_6\text{Ti}_2\text{Nb}_8\text{O}_{30}$ (BTN) has been known since 1968¹⁵ and consists of corner-sharing BO_6 octahedra (where $B = \text{Ti}$ and Nb), with peculiar Raman bands observed at about 260, 590, and 630 cm^{-1} .³ The resulting framework contains interstitial sites, indicated by C (4c point symmetry), that can accommodate up to four ions in the case of Li-substituted BTN compounds.¹⁶ The A sites are generally occupied by ions with a large coordination number.¹⁴ It is evident that, because of the large variety of ions that can occupy the A, B, and C sites, many compounds are expected to belong to this family.

In this work, pure and Fe-, Mn-, and Cr-substituted $\text{Ba}_6\text{Ti}_{2-x}\text{M}_x\text{Nb}_8\text{O}_{30}$ and Y- and Fe-substituted $\text{Y}_x\text{Ba}_{6-x}\text{Ti}_{2-x}\text{Fe}_x\text{Nb}_8\text{O}_{30}$ samples are synthesized. The influence of doping on the local structure, the doping cation valence state, the related defect formation, and the dielectric properties are investigated. To reach this goal, electron paramagnetic resonance (EPR), micro-Raman ($\mu\text{-R}$) spectroscopy, X-ray powder diffraction (XRPD), impedance spectroscopy (IS), and Seebeck coefficient (thermoelectric power) measurements as a function of temperature are carried out.

Experimental Methods

Pure and substituted BTN samples were prepared via solid-state synthesis from a mixture of BaCO_3 (Carlo Erba), TiO_2 (Merck, >99%), Nb_2O_5 (Aldrich, 99.99%), and Cr_2O_3 (Aldrich, 99.995%), MnO (Alfa, 99.5%), Y_2O_3 (Fluka, 99.9%), or Fe_2O_3 (Alfa, 99.9%) oxides in the proper amounts to obtain the required stoichiometry. The doping was performed by substituting Ti ions leading to the chemical formula $\text{Ba}_6\text{Ti}_{2-x}\text{M}_x\text{Nb}_8\text{O}_{30}$ ($M = \text{Fe}$, Cr , Mn ; $x = 0.06$ and 0.18) and Y and Fe on Ba and Ti, respectively, to obtain $\text{Ba}_{6-x}\text{Y}_x\text{Ti}_{2-x}\text{Fe}_x\text{Nb}_8\text{O}_{30}$ ($x = 0.18$). Each mixture was treated for 30 h at 1273 K, 30 h at 1423 K three times, and 30 h at 1473 K, with intermediate grinding. The powders were pelletized and treated for 15 h at 1473 K for the electrical characterization.

Room-temperature (RT) XRPD measurements were performed in air on a Bruker D5005 diffractometer with $\text{Cu K}\alpha$ radiation, a Ni filter, and a position-sensitive detector. Rietveld structural and profile refinement was carried out by means of the FULLPROF and TOPAS programs.^{17–18}

The IS measurements were performed by means of a frequency response analyzer Solatron 1260 apparatus in the frequency range of 10^{-3} – 10^7 Hz, with the experimental settings described elsewhere.¹⁹ Conductivity measurements were performed as a function of the temperature (up to 1173 K) on disk-shaped samples inserted in a polythermal electrochemical cell

* Corresponding author. Tel: +39-382-987203. Fax: +39-382-987575. E-mail: vincenzo.massarotti@unipv.it.

[†] "M. Rolla" dell'Università.

[‡] "A. Volta" dell'Università.

[§] CNR - IENI, Sezione di Pavia.

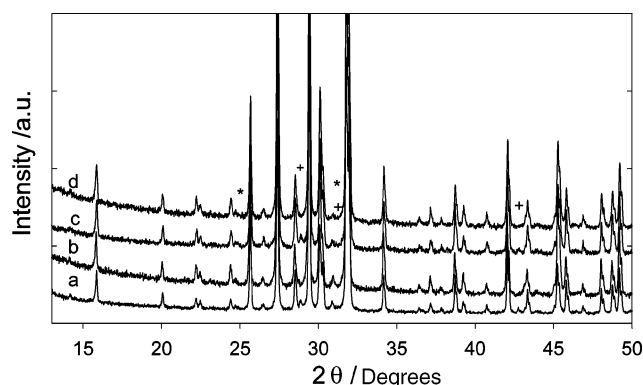


Figure 1. Comparison between the patterns of (a) pure, (b) $x_{\text{Fe}} = 0.06$, (c) $x_{\text{Cr}} = 0.06$, and (d) $x_{\text{Mn}} = 0.06$ doped BTN compounds. The * and + symbols indicate the main peaks of the $\text{Ba}_3\text{Ti}_4\text{Nb}_4\text{O}_{21}$ and $\text{Ba}_5\text{Nb}_4\text{O}_{15}$ impurity phases, respectively.

supplied by a guard circuit. To ensure good electrical contact for the conductivity measurements, platinum electrodes were deposited by sputtering on the opposite flat surfaces of the pellets. The samples were previously annealed at 1073 K for 6 h in O_2 or N_2 (<1 ppm O_2) flow and slowly cooled (5 K/min) to 573 K, the initial temperature for further measurements performed in suitable gas flow.

The RT dielectric constants were obtained by means of an “autobalance precision bridge” Wayne Kerr B311 capacity meter.

The Seebeck coefficient (α) measurements were performed up to 1200 K by means of the electrochemical cell already described.²⁰

EPR measurements were carried out at about 9.4 GHz at RT with a Bruker spectrometer. Particular care was taken in determining the sample mass and position in the resonant cavity to compare signal intensities (areas): different measurements on the same sample showed intensity variations of a few percent.

μ -R measurements were carried out at RT by using a Labram Dilor H10 spectrometer equipped with an Olympus microscope HS BX40. A HeNe laser beam (632.8 nm) was employed as an exciting light with a power of less than 10 mW at the sample. The microscope, coupled confocally to the spectrograph with a 100 \times objective of numerical aperture 0.9, collected the back-scattered Raman light from the sample irradiated with a laser spot of $\sim 1 \mu\text{m}$ diameter. The spectral resolution in the considered spectral range was $\sim 1 \text{ cm}^{-1}$.

Results

XRPD. The XRPD patterns show the typical lines of the BTN phase (JCPDS card no. 38-1329), independent of the type and content of dopant: as an example, in Figure 1, the patterns of pure and Fe-, Cr-, and Mn-doped ($x = 0.06$) BTN samples are compared. The peaks marked with * and + indicate the presence of small amounts of $\text{Ba}_3\text{Ti}_4\text{Nb}_4\text{O}_{21}$ ²¹ and $\text{Ba}_5\text{Nb}_4\text{O}_{15}$,²² respectively, quantified by a structural refinement by using the Rietveld method.^{17,18} The refined lattice parameters, atomic coordinates, and cation distribution, together with the percentage of the impurity phases pertinent to the different samples, are reported in Table 1; the discrepancy factors and the goodness of fit, indicating the reliability of the Rietveld refinements,¹⁷ are also given. The atomic coordinates are in agreement with data previously reported.¹⁴ The isotropic thermal factors, ranging between 0.1 and 2.0 \AA^2 , are reliable positive values. The occupancy factors pertinent to octahedral sites 1 and 2 are reported in Table 1; because of the very close atomic number

of Ti and the doping cations, the dopant amount has been included in the Ti occupancy factors during the refinement, therefore only the data for Ti and Nb are given in Table 1. The Nb percentage on site 2 is also reported. By refining the Y amount in the $x_{\text{Y,Fe}} = 0.18$ sample on the Ba sites (2a and 4c Wyckoff sites), it has been demonstrated that the total amount of Y is located on the 2a site. In Figure 2, experimental and calculated patterns of a typical Rietveld refinement ($x_{\text{Fe}} = 0.18$ sample) are shown.

EPR. The pure BTN samples, as expected, give no EPR signal. For Fe-doped samples, the EPR signal, shown in Figure 3a, is typical of Fe^{3+} ions in glass matrixes.²³ The same signal is observed in the Y- and Fe-substituted sample. This signal shows two components with $g_{\text{eff}} \sim 4.3$ and with $g_{\text{eff}} \sim 2$ whose origin can be attributed to Fe^{3+} ions in different site symmetries, that is, with different E and D crystal field parameter values, greater or lower than $h\nu$, appearing in the standard spin Hamiltonian. The relative intensity of the $g_{\text{eff}} \sim 4.3$ component decreases upon increasing the dopant amount.²³ Moreover, as previously reported,²⁴ for small Fe^{3+} doping levels, the intensity ratio of the two components is nearly linear with concentration if dipolar interactions on the line broadening are taken into account only for the $g_{\text{eff}} \sim 4.3$ component.

The Mn-doped samples show an EPR signal with $g_{\text{eff}} \geq 2$, which is very similar to that of the Mn^{2+} signals in a glass matrix (Figure 3b).²³ The signal areas, calculated by numerical double integration and compared with a standard sample, are substantially congruent with the Mn concentration ($x_{\text{Mn}} = 0.06$ and $x_{\text{Mn}} = 0.18$) in the samples.

In the case of the Cr-doped samples, the EPR signal (Figure 3c) consists at least of three components with $1.95 < g < 1.98$, is assigned to Cr^{3+} ions in different octahedral sites,²⁵ and, due to the $1/2 \leftrightarrow -1/2$ transition, is poorly sensitive to the site symmetry axes orientation with respect to the applied magnetic field. A signal deconvolution by numerical methods is shown in Figure 4 for the $x_{\text{Cr}} = 0.06$ sample. From the signal areas evaluation, the following occupancy percentage for the three sites is obtained: site 1, $\sim 94\%$; site 2, $\sim 5\%$; site 3, $\sim 1\%$. Similar deconvolution for the $x_{\text{Cr}} = 0.18$ sample leads to the following results: site 1, $\sim 90\%$; site 2, $\sim 9\%$; site 3, $\sim 1\%$.

Micro-Raman. In Figure 5 the μ -R spectra of pure and $x = 0.06$ Fe-, Mn-, and Cr-doped BTN samples are reported in the energy region of 100–1000 cm^{-1} , and the related peak positions are listed in Table 2. The Raman scattering of the samples is characterized by two main broadened features centered at $\sim 245 \text{ cm}^{-1}$ and $\sim 610 \text{ cm}^{-1}$, in good agreement with those reported in a recent paper.³ In addition, three Raman bands can be clearly recognized below 200 cm^{-1} , even if the shape of the spectra can be affected by the cut of a notch filter. Above 200 cm^{-1} , the Raman bands in the BTN samples are broadened with respect to those reported for $\text{Ba}_2\text{Na}_{1-x}\text{Nd}_x\text{Nb}_5\text{O}_{15}$,²⁶ which crystallizes with the same tetragonal symmetry. The doping does not markedly affect the Raman response. Indeed, an analysis of the different Raman bands, carried out by interpolating the data with the overlapping of different Lorentzian curves, shows that the changes in peak position of the main Raman modes are very small with respect to the pure compound and, in some cases, are on the order of experimental accuracy (Table 2). For only Cr-doped samples, a reduced Raman efficiency and a very strong luminescence, maybe due to Cr^{3+} radiative transitions, are observed at higher energy (see inset in Figure 5).

Concerning the presence of impurity phases, μ -R spectra did not show the main peaks pertinent to the compounds $\text{Ba}_5\text{Nb}_4\text{O}_{15}$ ²⁷ and $\text{Ba}_3\text{Ti}_4\text{Nb}_4\text{O}_{21}$; indeed, the Raman spectra of these phases

TABLE 1: Lattice Parameters, Atomic Coordinates, Cation Distribution, and Impurity Phases Percentages Obtained by Rietveld Refinement^{18,a}

	$x = 0.0$	$x_{\text{Fe}} = 0.06$	$x_{\text{Fe}} = 0.18$	$x_{\text{Cr}} = 0.06$	$x_{\text{Cr}} = 0.18$	$x_{\text{Mn}} = 0.06$	$x_{\text{Mn}} = 0.18$	$x_{\text{Y,Fe}} = 0.18$
XRPD								
R_{wp}	5.31	4.31	4.15	4.40	4.36	8.95	4.37	4.29
R_{p}	4.04	3.28	3.15	3.38	3.34	6.99	3.33	3.34
Gof	1.45	1.41	1.39	1.37	1.34	1.41	1.41	1.27
$a/\text{\AA}$	12.530(1)	12.528(2)	12.538(2)	12.532(2)	12.535(1)	12.529 (2)	12.537(2)	12.527(2)
$c/\text{\AA}$	4.0047(7)	4.0030(6)	3.9989(6)	4.0047(7)	3.9996(5)	4.0044(5)	4.0029(6)	3.9907(1)
Ba1: x	0.0	0.0	0.0	0.0	0.0	0.0	0.0	0.0
y	0.0	0.0	0.0	0.0	0.0	0.0	0.0	0.0
z	0.0	0.0	0.0	0.0	0.0	0.0	0.0	0.0
Ba2: x	0.1720(1)	0.1719(1)	0.1717(1)	0.1714(1)	0.1717(1)	0.1714(1)	0.1715(1)	0.1720(1)
y	0.6720(1)	0.6719(1)	0.6717(1)	0.6714(1)	0.6717(1)	0.6714(1)	0.6715(1)	0.6720(1)
z	0.990(4)	0.976(3)	0.984(3)	0.991(6)	0.988(3)	0.999(4)	0.981(3)	0.970(3)
Ti1, Nb1	0.0	0.0	0.0	0.0	0.0	0.0	0.0	0.0
	0.5	0.5	0.5	0.5	0.5	0.5	0.5	0.5
	0.452(3)	0.461(3)	0.454(3)	0.471(5)	0.457(3)	0.442(3)	0.445(3)	0.453(3)
Ti2, Nb2	0.0743(2)	0.0748(2)	0.0747(2)	0.0747(2)	0.0744(2)	0.0745(2)	0.0752(2)	0.0745(2)
	0.2153(2)	0.2155(2)	0.2151(2)	0.2150(2)	0.2151(2)	0.2145(2)	0.2151(2)	0.2149(2)
	0.487(3)	0.472(3)	0.489(3)	0.488(5)	0.481(3)	0.478(4)	0.474(3)	0.457(2)
O1	0.0	0.0	0.0	0.0	0.0	0.0	0.0	0.0
	0.5	0.5	0.5	0.5	0.5	0.5	0.5	0.5
	0.024(7)	0.059(9)	0.041(18)	0.060(9)	0.070(13)	0.031(11)	0.040(22)	0.022(13)
O2	0.284(1)	0.281(1)	0.280(1)	0.286(1)	0.276(1)	0.278(1)	0.280(1)	0.283(1)
	0.784(1)	0.781(1)	0.780(1)	0.786(1)	0.776(1)	0.778(1)	0.780(1)	0.783(1)
	0.556(8)	0.532(10)	0.540(10)	0.515(11)	0.551(10)	0.525(10)	0.533(11)	0.529(10)
O3	0.074(1)	0.072(1)	0.072(1)	0.074(1)	0.073(1)	0.074(1)	0.076(1)	0.075(1)
	0.211(1)	0.210(1)	0.213(1)	0.214(1)	0.212(1)	0.213(1)	0.211(1)	0.212(1)
	0.990(10)	0.984(11)	0.988(12)	0.995(10)	0.987(13)	0.986(13)	0.999(13)	0.984(12)
O4	0.344(1)	0.343(1)	0.344(1)	0.342(1)	0.346(1)	0.343(2)	0.347(1)	0.343(1)
	0.002(1)	0.008(1)	0.008(1)	0.010(1)	0.005(1)	0.001(1)	0.007(1)	0.006(1)
	0.550(6)	0.512(7)	0.518(7)	0.515(9)	0.525(8)	0.520(10)	0.536(7)	0.505(9)
O5	0.135(1)	0.134(1)	0.135(1)	0.139(1)	0.136(1)	0.143(1)	0.137(1)	0.137(1)
	0.069(1)	0.071(1)	0.072(1)	0.065(1)	0.073(1)	0.074(1)	0.074(1)	0.072(1)
	0.525(9)	0.514(10)	0.507(9)	0.516(11)	0.521(13)	0.503(11)	0.501(13)	0.509(12)
site 1 Ti	0.766	0.708	0.697	0.539	0.810	0.645	0.771	0.737
Nb	1.234	1.292	1.303	1.461	1.190	1.355	1.229	1.263
site 2 Ti	1.234	1.292	1.303	1.461	1.190	1.355	1.229	1.263
Nb	6.766	6.708	6.697	6.539	6.810	6.645	6.770	6.737
% Nb (site 2)	84.6	83.9	83.7	81.7	85.1	83.1	84.6	84.2
% Ba ₃ Nb ₄ Ti ₄ O ₂₁	4(1)	3.2(0.6)	2.0(0.4)	3.2(1.0)	3.4(0.6)	—	—	3.7(0.8)
% Ba ₅ Nb ₄ O ₁₅	—	—	—	2.3(0.6)	—	1.8(0.2)	2.8(0.7)	0.2(0.2)
dielectric constants								
ϵ_{r}	83.6	89.2	430.0	107	140	81.6	80.5	1550

^a The discrepancy factors and the goodness of fit¹⁷ are also given. In the last row, the dielectric constant ϵ_{r} is also reported.

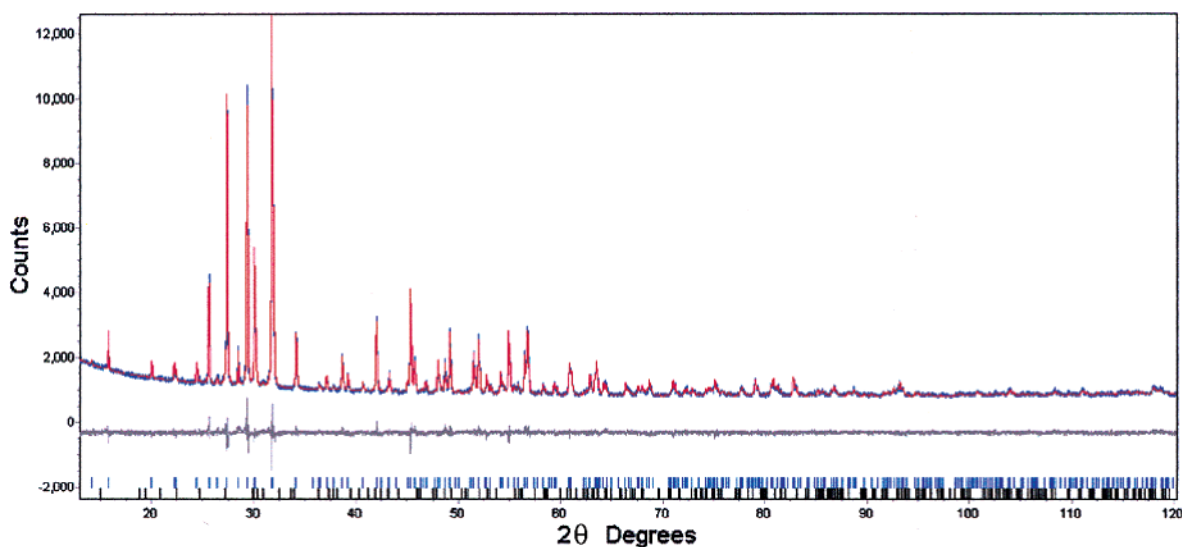


Figure 2. Example of a typical Rietveld refinement plot ($x_{\text{Fe}} = 0.18$). The experimental data (blue) are compared with the calculated (red) line. At the bottom, the difference curve and the bars indicating the reflection positions of the two refined phases are also reported.

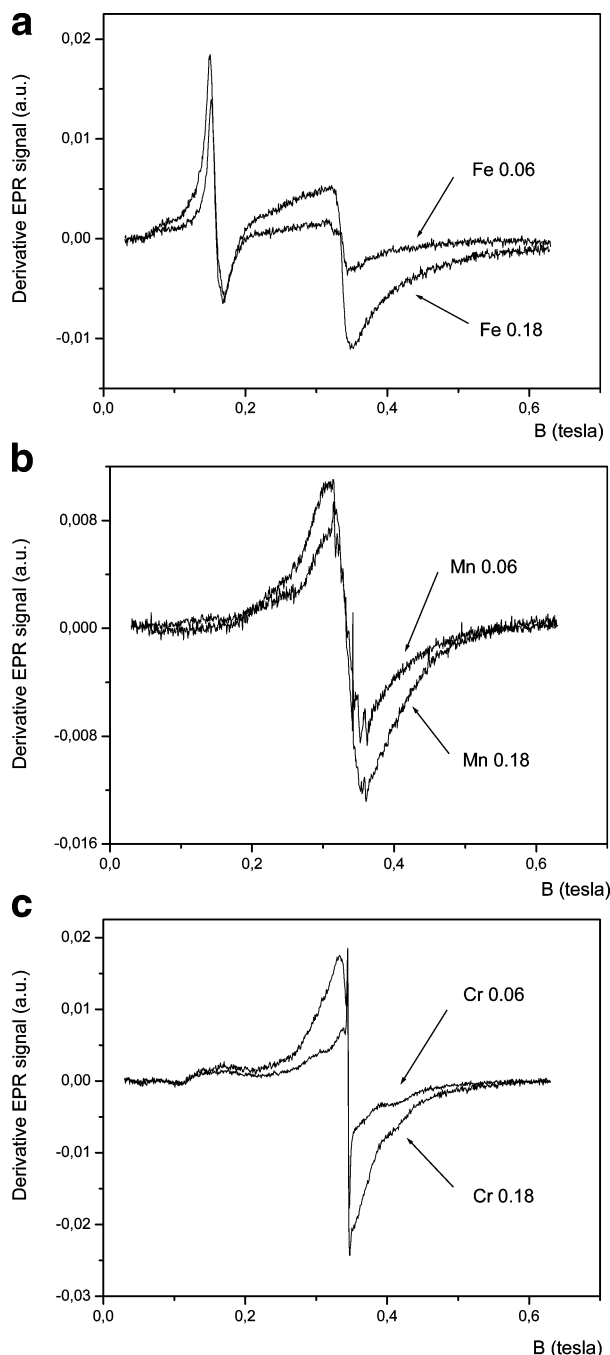


Figure 3. EPR spectra of (a) Fe-, (b) Mn-, and (c) Cr-doped samples.

are very similar to that of BTN and prevent their identification in the amount deduced by XRPD.

IS. The pure and Fe-doped sample IS plots collected at 823 K are reported in Figure 6a. A significant decrease in resistivity upon increasing the dopant amount is observed. In the inset of Figure 6a, it is shown that the reducing N_2 flow produces at the same temperature a decrease in the resistivity of the $x_{\text{Fe}} = 0.18$ sample of about 3 orders of magnitude. Each sample in the high-frequency region shows only one well-developed semicircle associated with the resistivity bulk contribution. A little overlapped and depressed arc at lower frequencies is attributed to the grain boundary effect. In Figure 6b, the impedance plots pertinent to the $x_{\text{Cr}} = 0.06$ and 0.18 samples are compared with the pure sample behavior, while, in Figure 6c, the impedance plot of the $x_{\text{Mn}} = 0.06$ sample is reported. From the data of the $x_{\text{Mn}} = 0.18$ sample given in the inset, it is

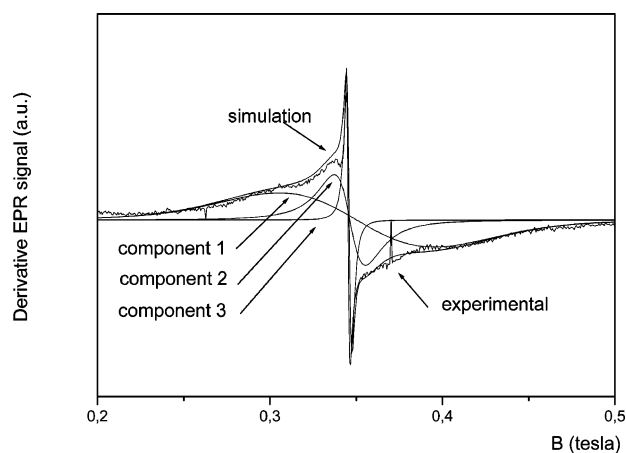


Figure 4. EPR signal deconvolution by numerical methods for the $x_{\text{Cr}} = 0.06$ sample.

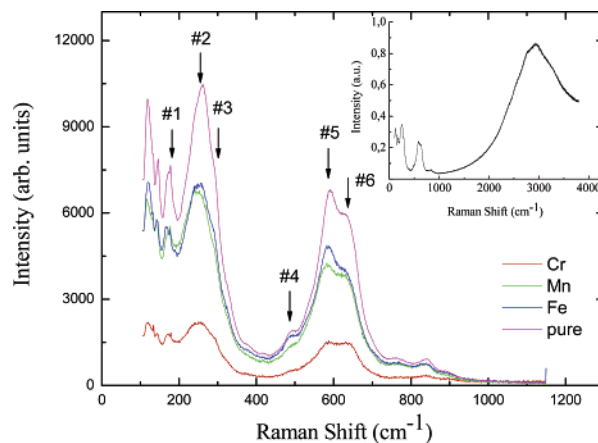


Figure 5. Raman spectra of pure and $x = 0.06$ Fe-, Mn-, and Cr-doped BTN samples in the energy region of 100–1000 cm^{-1} ; in the inset, the Raman spectrum of a Cr-doped BTN sample in the energy region of 100–3800 cm^{-1} is shown.

TABLE 2: Raman Peak Positions for Pure and $x = 0.06$ Fe-, Mn-, and Cr-Doped BTN Samples^a

Raman modes (see Figure 7)	peak position (cm^{-1})			
	pure	Fe	Mn	Cr
#1	173.3	166.9	172.0	170.0
#2	263.2	258.6	257.9	256.7
#3	294.3	292.2	292.8	293.2
#4	491.3	490.8	490.8	491.2
#5	588.6	583.6	579.1	584.9
#6	641.6	639.5	636.7	641.6

^a The instrumental spectral resolution in the observed spectral range is $\sim 1 \text{ cm}^{-1}$. The uncertainty derived from the fitting procedure ranges between 0.2 and 0.3 cm^{-1} .

found that the resistivity is more than 1 order of magnitude lower than that of $x_{\text{Mn}} = 0.06$. In Cr-doped (Figure 6b) and $x_{\text{Mn}} = 0.06$ (Figure 6c) samples, the observed half circle is markedly asymmetric and can be explained by the convolution of two distinct bulk contributions. A well-developed half circle is instead observed for the $x_{\text{Mn}} = 0.18$ sample. In Figure 7a,b, the impedance plots at 873 K of the pure and $x_{\text{Fe}} = 0.18$ samples in air and N_2 flow are shown. The effect of the N_2 reducing atmosphere is remarkable in both samples. The IS plots at 823 K (Figure 6) show that the increasing Fe doping enables a resistivity decrease, while, in the case of Cr and Mn substitutions, the resistivity increases for $x = 0.06$ and decreases for $x = 0.18$.

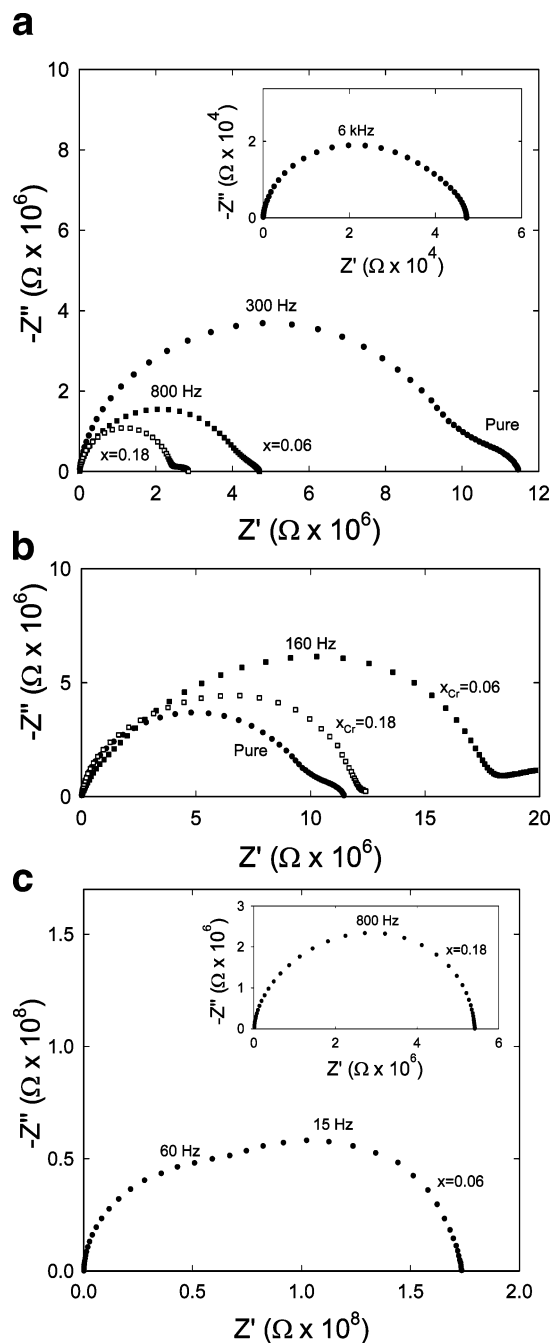


Figure 6. IS plots at 823 K of (a) pure and Fe-doped, (b) pure and Cr-doped, and (c) Mn-doped BTN samples; in panel a, the inset shows the IS plot of the $x_{\text{Fe}} = 0.18$ sample in reducing atmosphere at the same temperature.

The bulk conductivity contribution for all the samples in the range of 773–1073 K is shown in the Arrhenius plot of Figure 8. The σ values obtained in N_2 flow for pure BTN, $x_{\text{Y,Fe}} = 0.18$, and $x_{\text{Fe}} = 0.18$ samples are the highest.

The Seebeck coefficient α determined in the temperature range of 873–1170 K for pure and doped samples suggests the negative nature of the charge carriers. The results for $x_{\text{M}} = 0.18$ are shown in Figure 9. A monotonic decrease between -140 and $-440 \mu\text{V/K}$ with increasing temperature can be observed; less negative α values are obtained for the doped samples with respect to the pure BTN sample, except for the case of a balanced Y, Fe sample, whose trend is very similar to that of the pure one.

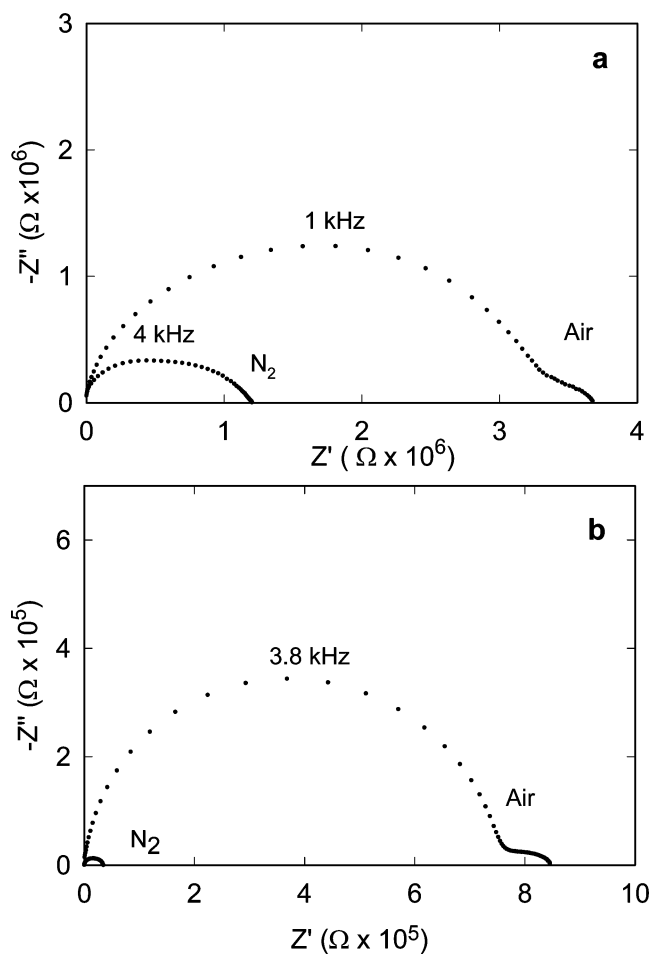


Figure 7. IS plots at 873 K of (a) pure and (b) $x_{\text{Y,Fe}} = 0.18$ doped BTN samples.

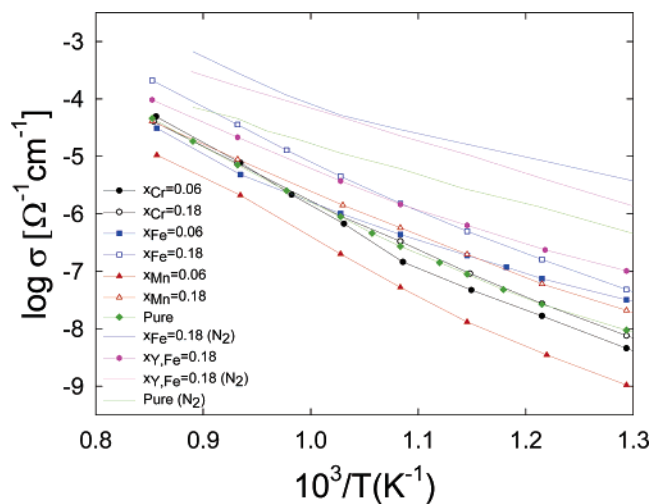


Figure 8. Arrhenius plots of all the samples in the temperature range of 773–1073 K. The $x_{\text{Fe}} = 0.18$, $x_{\text{Y,Fe}} = 0.18$, and pure sample data collected in N_2 flow are also reported.

The dielectric constants ϵ_r at RT are reported in Table 1; the type and amount of the dopant ion significantly influence the ϵ_r value.

Discussion

The values of the a and c lattice parameters reported in Table 1 reveal, with doping, a slight increase and decrease, respectively, leading to an approximately constant value of the cell

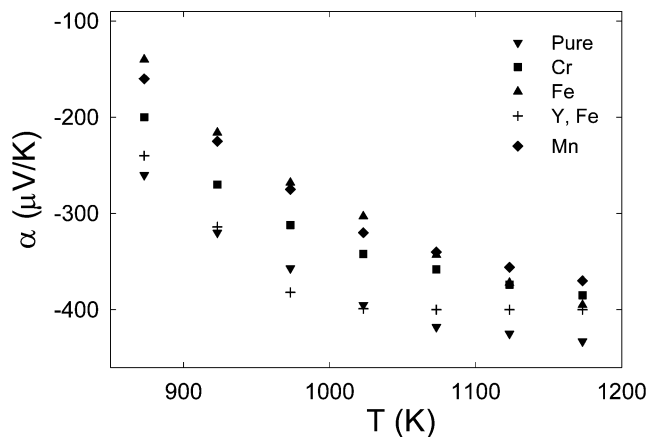


Figure 9. Seebeck coefficient α as a function of temperature for pure and doped ($x_M = 0.18$) BTN samples.

volume, independent of the type and amount of substitution. A random distribution of Ti and Nb on the two octahedral sites (Table 1) is found by the Rietveld refinement of occupancy factors, in agreement with data previously reported;¹⁴ in particular, we have determined that the Nb percentage on site 2, which also represents the percentage of the total Nb amount, ranges between 81.7 and 85.1%, demonstrating an approximately constant cation distribution, independent of doping.

Concerning the valence state of the doping ions and their distribution on the BTN cation sites, interesting information has been obtained by EPR signals. In the case of Fe-doped samples, two main EPR signals attributed to Fe³⁺ ions are obtained with $g_{\text{eff}} = 4.3$ and $g_{\text{eff}} = 2$; this suggests that Fe³⁺ cations occupy at least two different environments, such as the two octahedral sites present in the BTN structure. From the XRPD refinements, a constant Ti/Nb ratio on the two sites is obtained (see Table 1). In addition, the EPR results suggest the following considerations: for the signal components, we assumed that the areas $A \propto (\Delta H)^2 I$, with ΔH being the line width and I being the derivative signal intensity, were proportional to the concentration $c = n/V$, with n being the number of dopant ions in a spherical volume V with radius r . We verified that ΔH_2 was actually independent of c , being the $g = 2$ component, which is an envelope of many signals around $g = 2$. By supposing that, for small concentrations, only dipolar interactions contribute to $\Delta H_{4.3}$, we can write $\Delta H_{4.3} = k + \alpha c$, with k being the contribution to the line width, independent of c , the dipolar interaction energy.

$$E = \frac{1}{r^3} [\vec{\mu}_1 \cdot \vec{\mu}_2 - 3\mu_{1z}\mu_{2z}] \quad (1)$$

By supposing that the ratio between the two areas (the same distribution in the different sites for different c) might be constant, we can write

$$\frac{A_{4.3}}{A_2} \propto \frac{(k^2 + 2k\alpha c + \alpha^2 c^2) I_{4.3}}{(\Delta H_2)^2 I_2} = K \quad (2)$$

and finally

$$\frac{I_2}{I_{4.3}} = (A + Bc + Cc^2) \quad (3)$$

with A , B , and C being constant parameters related to k , K , α , and ΔH_2 . For very small concentrations ($Cc^2 \ll Bc$), the intensity ratio $I_2/I_{4.3}$ behaves nearly linear with c , as experimentally

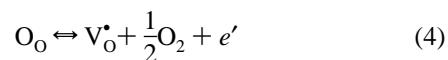
observed. On this basis, we can understand that the Fe³⁺ occupation of each crystallographic site is proportional to the total amount x_{Fe} .

The EPR signals of the Mn-doped samples can be attributed to Mn²⁺ cations distributed on both octahedral sites. Moreover, from the signal areas, it can be deduced that 2+ is the only oxidation state of the Mn ions in the samples.

More quantitative results on Cr distribution in the BTN samples can be obtained by analyzing the EPR signal as given in the Results section. On the basis of signal simulation, three main components can be observed (Figure 4), as the result of Cr³⁺ ions in three octahedral environments, one of them significantly occupied (~ 94 and $\sim 90\%$ for $x_{\text{Cr}} = 0.06$ and $x_{\text{Cr}} = 0.18$, respectively). The lowest occupied site ($\sim 1\%$ Cr in both doped samples) could be assigned to octahedral environments of the impurity phases (see Table 1). A Cr distribution in good agreement with the EPR results (90% on site 1 and 10% on site 2 in both doped samples) has been obtained by additional Rietveld refinement of XRPD data on the basis of a compositional model starting from equal distribution of Cr³⁺ on the two octahedral sites.

To interpret the conductivity results, we remember that, for all the samples, the negative thermoelectric power (α) indicates a whole negative charge responsible for the conducting process: the most negative values are obtained for pure and Y, Fe samples. Additionally, the valence states of the Fe³⁺, Cr³⁺, and Mn²⁺ ions and their distribution on the octahedral sites were found by EPR and XRPD measurements; moreover, the Y³⁺ occupancy on the Ba²⁺ ($2a$) site has been determined by XRPD Rietveld analysis and agrees with previous crystallochemical considerations.^{7,12} So, because of the difference in the oxidation state between dopant and substituted cations, a suitable defect model, consisting of oxygen vacancies, electrons, or holes, able to maintain the charge balance in the system must be considered for each doping system, and the equilibrium charge concentration should result in agreement with the observed transport behavior.

The Fe-doped samples display, in the whole temperature range, higher conductivity values than the pure one, more evident for higher Fe content (Figure 8). The σ versus $1/T$ behavior is rather complex and does not allow a simple correlation with the dopant charge and content. Nevertheless, the conductivity results as a function of p_{O_2} at a constant temperature suggest a possible defect model constituted by electrons and oxygen vacancies according to the “quasi-chemical” equilibrium written following the Kroger and Vink formalism:



where the thermodynamic constant is

$$K(T) = |e'| |\text{V}_\text{O}^\bullet| p_{\text{O}_2}^{1/2} \quad (5)$$

and finally, in an intrinsic system with $|e'| = \text{V}_\text{O}^\bullet$,

$$|e'| \propto p_{\text{O}_2}^{-1/4} \propto \sigma \quad (6)$$

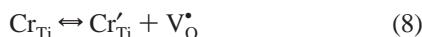
In N₂ flow, with $p_{\text{O}_2} \approx 1 \times 10^{-6}$ atm, a significantly greater contribution of $|e'|$ and $\text{V}_\text{O}^\bullet$ to the charge transport can be considered, at a given temperature, in agreement with the much greater σ value with respect to the results in air.

The substitution by cations with an oxidation state lower than that of Ti⁴⁺ should be balanced by electron holes in the

conduction band that contribute to a σ increase and a less negative Seebeck coefficient (Figure 9). In other words, the doping ion acts as an acceptor, according to



In other cases, for example, for Cr^{3+} and, more remarkably, for Mn^{2+} doping, a competing charge balance mechanism could take place in addition to or in substitution of an equilibrium analogous to eq 7. For example, oxygen vacancy formation may be considered:



On the basis of this equation, the $\text{V}_{\text{O}}^{\bullet}$ increase causes a decrease in the $|e'|$ concentration, decreasing the σ values, at least for $10^3/T > 1$, as observed in Figure 8. The $x_{\text{Cr}} = 0.18$ sample shows a conductivity trend similar to that of the pure BTN sample in the whole temperature range, indicating a substantial balance between the competing defect equilibria. For $10^3/T < 1$, all the $x = 0.06$ doped samples show a common σ trend, except for the Mn-doped one, which shows lower σ values in the whole temperature range. For Mn^{2+} substitution on Ti sites, the defect model should take into account that a double excess charge should be paired to the point defect that compensates a double concentration of oxygen vacancies:

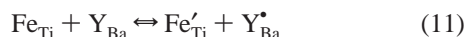


A double concentration of $\text{V}_{\text{O}}^{\bullet}$ can explain the greater decrease in $|e'|$ and in σ . The $x_{\text{Mn}} = 0.18$ sample shows greater σ values with respect to the pure sample for $10^3/T > 1$, so we hypothesize that high Mn^{2+} concentrations may also create different mobile charges, such as holes, able to explain the observed results.

For the samples doped with Fe and Y (same amount) on Ti^{4+} and Ba^{2+} sites, respectively, the presence of both equilibrium 7 and



could be taken into account. So, the whole equilibrium is



On this basis, eq 4 should be predominant and could explain the α values of the Y,Fe-doped sample, which are very similar to that of the pure one. In other words, the substituted centers Fe'_{Ti} and Y'_{Ba} may be able to separate electrons and holes under an applied electric field, in addition to the free carriers of eq 4. On this ground, we can expect an increase in carriers, in agreement with higher σ values with respect to the pure sample.

The defect models described above can explain both the σ differences among the samples with the different doping cations (Fe^{3+} , Cr^{3+} , Mn^{2+} and Y^{3+} , Fe^{3+}) and the σ differences observed for different p_{O_2} values. In fact, according to eqs. 4–6, the slope of the $\log \sigma$ versus $\log p_{\text{O}_2}$ plot is expected to approach the value $-1/4$. On the basis of the conductivity values reported in the Arrhenius plot of Figure 8, pure BTN, $x_{\text{Fe}} = 0.18$, and $x_{\text{Y,Fe}} = 0.18$ samples give, in the temperature range of 873–973 K, $-0.25(4)$, $-0.24(6)$, and $-0.22(2)$, respectively. These results confirm that the electrons are the mobile charge carriers.

Concerning the dielectric constant, ϵ_r , a significant increase is obtained in Fe- and Y,Fe-doped samples with respect to that of pure BTN (Table 1). It can be well observed that the dopant ion can play a relevant role in optimizing the dielectric properties

of BTN materials. Moreover, the double bulk effect, observed on $x_{\text{Mn}} = 0.06$ and Cr-doped samples in the IS plots, can be explained by the coexistence of particles displaying two different morphologies, as evidenced by SEM observations.

To complete the characterization of our samples, some comments on μ -R measurements can be added. The RT complex μ -R spectrum of the BTN compound (Figure 5), may be considered peculiar for the compounds that crystallize in the tetragonal SG *P4bm*. Two main vibrational units, that is, TiO_6 and NbO_6 octahedra,^{3,14} must be considered in a non-centrosymmetric system in which the resulting active Raman modes should be of *E* and *A1* type, which result from the *F* modes when the structure undergoes the ferroelectric phase transition at about 408 K.³ In particular, close similarity may be observed by comparing the Raman features from systems constituted by octahedral units of NbO_6 , such as LiNbO_3 in the region around 600 cm^{-1} , usually ascribed to TO phonon modes.²⁹ Furthermore, by comparing our spectra with that of BaTiO_3 ,²⁸ a very close similarity is noticeable. As known, the RT μ -R spectrum of BaTiO_3 (ferroelectric, tetragonal crystal structure) is characterized by the presence of intense second-order and/or higher order Raman signals with two main features centered at $\sim 250 \text{ cm}^{-1}$ and at $\sim 540 \text{ cm}^{-1}$, in the same energy region of the bands we observed in BTN samples. The Raman signals in the lower energy range ($< 200 \text{ cm}^{-1}$) can be attributed to external vibrations of NbO_6 and TiO_6 units, as reported in ref 26, but we cannot exclude an active role of vibrations involving the oxygen polyhedra around the Ba ions. In conclusion, the resulting μ -R spectrum of the BTN system may be seen as a mixing of different first-order Raman structures, caused by internal and external vibrations of BO_6 octahedral units, with second- (or higher) order features.

Conclusions

The tungsten bronze BTN framework displays a “sponge”-like behavior, related to the availability of the different cationic sites to host suitable doping ions, as verified by EPR data, without modifying the cell volume and structure, as deduced from XRPD and μ -R results.

We verified the influence of cation doping on the local structure, the oxidation state of the substituted cations, and the possible defect formation able to maintain the lattice charge neutrality by spectroscopic, structural, and transport measurements. Starting from the valence state of the doping ions Fe^{3+} , Cr^{3+} , and Mn^{2+} , determined by EPR, and from the thermoelectric power results, evidencing a negative charge transport, different charge-compensating defect equilibria have been proposed. The creation of oxygen vacancies and electrons or substituted ions and positive electron holes or electrons based on the pertinent equilibria are used to interpret the conductivity results in air and N_2 flow in a wide temperature range. Finally, we also observed the relevant role of doping in improving the dielectric properties of BTN materials, especially in the case of Y,Fe charge balanced substitution.

References and Notes

- (1) Roberts, G. L.; Cava, R. J.; Peck, W. F., Jr.; Krajewski, J. J. *J. Mater. Res.* **1997**, *12*, 526.
- (2) Itoh, Y.; Iwasaki, H. *J. Phys. Chem. Solids* **1973**, *34*, 1639.
- (3) Yuan, Y.; Chen, M.; Wu, Y. J. *J. Appl. Phys.* **2005**, *98*, 84110-1.
- (4) Neurgaonkar, R. R.; Nelson, J. G.; Oliver, J. R. *Mater. Res. Bull.* **1992**, *27*, 677.
- (5) Rao, P. P.; Ghosh, S. K.; Koshy, P.; Warriar, K. G. K. *J. Mater. Sci. Lett.* **2003**, *22*, 217.
- (6) Zheng, X. H.; Chen, X. M. *J. Mater. Res.* **2002**, *17*, 1664.

- (7) Palai, R.; Choudhary, R. N. P.; Tewari, H. S. *J. Phys. Chem. Solids* **2001**, *62*, 695.
- (8) Rao, K. S.; Subrahmanyam, A. S. V.; Viswarupachary, P. *Ferroelectrics* **1998**, *215*, 95.
- (9) Sun, Y. H.; Chen, X. M.; Zheng, X. H. *J. Appl. Phys.* **2004**, *96*, 7435.
- (10) Shimazu, M.; Tsukioka, M.; Mitobe, N.; Kuroiwa, S.; Tsutsumi, S. *J. Mater. Sci.* **1990**, *25*, 4525.
- (11) Sapriel, J.; Boudou, A. *Ferroelectrics* **1978**, *21*, 323.
- (12) Iwasaki, H. *Mater. Res. Bull.* **1971**, *6*, 251.
- (13) Tribotté, B.; Haussonne, J. M.; Desgardin, G. *J. Eur. Ceram. Soc.* **1999**, *19*, 1105.
- (14) Chi, E. O.; Gandini, A.; Ok, K. M.; Zhang, L.; Halasyamani, P. S. *Chem. Mater.* **2004**, *16*, 3616.
- (15) Jamieson, P. B.; Abrahams, S. C. *Acta Crystallogr., Sect. B* **1968**, *24*, 984.
- (16) Abrahams, S. C.; Jamieson, P. B.; Bernstein, J. L. *J. Chem. Phys.* **1971**, *54*, 2355.
- (17) Rodriguez Carvajal, J. *Physica B* **1993**, *192*, 55.
- (18) Bruker AXS 2000: TOPAS V2.1; General profile and structural analysis software for powder diffraction data; User Manual Bruker AXS: Karlsruhe, Germany, 2000.
- (19) Chiodelli, G.; Lupotto, P. *J. Electrochem. Soc.* **1991**, *9*, 2703.
- (20) Chiodelli, G.; Flor, G.; Scagliotti, M. *Solid State Ionics* **1996**, *91*, 109.
- (21) Groult, D.; Chailleux, J. M.; Choynet, J.; Raveau, B. *J. Solid State Chem.* **1976**, *19*, 235.
- (22) Pagola, S.; Polla, G.; Leyva, G.; Casais, M. T.; Alonso, J. A.; Rasines, I.; Carbonio, R. E. *Mater. Sci. Forum* **1996**, *228*, 819.
- (23) Griscom, D. L. *J. Non-Cryst. Solids* **1980**, *40*, 211 and references therein.
- (24) Azzoni, C. B.; DiMartino, D.; Marchesi, V.; Messiga, B.; Riccardi, M. P. *Archaeometry* **2005**, *47*, 383.
- (25) Abragam, A.; Bleaney, B. *Electron Paramagnetic Resonance of Transition Ions*; Clarendon Press: Oxford, 1970; pp 430–434.
- (26) Xia, H.-R.; Li, L. X.; Yu, H.; Meng, X.-L.; Zhu, L.; Hu, L.-J. *Cryst. Res. Technol.* **1999**, *34*, 901.
- (27) Massa, N. E.; Pagola, S.; Carbonio, R. *Phys. Rev. B* **1996**, *53*, 8148.
- (28) Di Domenico, M.; Wemple, S. H.; Porto, S. P. S. *Phys. Rev.* **1968**, *174*, 522.
- (29) Schaufele, R. F.; Weber, M. J. *Phys. Rev.* **1966**, *152*, 705.